Numerical Modeling of Hydraulic Stimulation and Long-Term Fluid Circulation at the Utah FORGE Project

Mark W. McClure[1], Rohan Irvin[1], Kevin England[2], and John McLennan[3]

[1]ResFrac Corporation, www.resfrac.com

[2] E-K Petro Consulting LLC

[3] University of Utah

Corresponding author: mark@resfrac.com

Keywords: Enhanced Geothermal Systems, FORGE, hydraulic fracturing, modeling, thermal drawdown, CO2, flow conformance

ABSTRACT

In the coming months, the Utah FORGE project plans to connect two vertically offset inclined wells – 16A and 16B – using multistage hydraulic fracturing. Six fracturing stages will be performed, varying: fluid type, cluster spacing, flow rate, total volume, and (possibly) proppant type. In this paper, we perform numerical simulations of these stimulations to predict: fracture geometry, the number of frac hits that will be observed in the DAS fiber at the production well (16B), the flow rate that will be achieved during initial circulation tests, and the thermal drawdown that will occur during long-term circulation tests. The simulation model is calibrated to the fracture geometry observations from the previously performed Stage 3 (consisting of cross-linked gel) in the 16A well. The upcoming stimulations will provide an opportunity to test model predictions and assumptions. In addition to the Base Case model, we run sensitivity analysis simulations varying key model inputs. The results show that the number of frac hits (and the ultimate connectivity between the wells) depends on the effective fracture toughness and the fracture conductivity during propagation. Simulations suggest that thermoelastic stress effects have potential to cause early thermal breakthrough during circulation. A simulation is performed using inflow control at the production well (and including thermoelastic stress reduction), and it shows that inflow control can prevent premature breakthrough and cause thermoelastic stress to have a positive, rather than negative effect, on overall thermal extraction. Finally, a simulation is performed circulating CO_2 instead of water. The net effect of using CO_2 is a moderate increase in the rate of thermal extraction, caused by the differences in viscosity, density, and heat capacity.

1. INTRODUCTION

The U.S. Department of Energy's (U.S. DOE) Frontier Observatory for Research in Geothermal Energy (FORGE) is a collaborative field-scale project focused on developing and testing technologies for Enhanced Geothermal Systems (EGS) (Moore et al., 2023). Alongside recent projects from Fervo Energy (Norbeck and Latimer, 2023), the project is differentiated from past EGS projects because it utilizes multistage fracturing along highly deviated wellbores. Modeling and reservoir engineering studies predict that this approach should achieve dramatically improved performance (Glauser et al., 2013; Shiozawa and McClure, 2014; Lowry et al., 2014; McClure et al., 2022), and early results from field trials confirm this prediction (Norbeck and Latimer, 2023).

Previously, three small-scale, mostly proppantless fracturing treatments were performed at FORGE in Well 16A (Stages 1, 2, and 3). Stage 1 was openhole, and Stages 2 and 3 were cased and cemented, with a single perforated interval. In the coming months, six additional fracturing stages are planned in 16A (Stages 4-9), using a variety of cluster spacings, cluster counts, and fluid types. All stages will be fractured with plug and perf limited-entry completions and proppant. The goal will be to develop conductive flow pathways between Well 16A and the more recently drilled (and not stimulated) 16B. The anticipated stage designs are summarized in Table 1.

After the fracturing of Well 16A, the 16B will be perforated and stimulated with relatively small-scale fracturing treatments (probably including proppant). The objective of the 16B treatments will be to break down the cement sheath, create annular pathways, and connect with the fractures created by the 16A stimulations. Subsequently, circulations tests will be performed to evaluate connectivity between the wells.

The FORGE project is designed as a full-scale, practical laboratory, not as a commercial project. Thus, the stimulation design was selected to provide variability in parameters such as cluster spacing, cluster count, and fluid type. A variety of field diagnostics will be deployed, and it will be possible to measure the impact of these design changes. There are a variety of other differences between the FORGE project and a commercial project. For example, the well spacing and configuration has not been optimized to maximize economic performance (by considering the tradeoff between thermal longevity and flow rate, as discussed by McClure et al. 2022).

Table 1: Planned fracture treatment designs for Stages 4-8 in Well 16A at Utah FORGE (England and McLennan, 2023).

Well	Stage Name	Number of Clusters	Fluid Type	Fluid Volume (bbl)	Pump Rate (bpm)	100-mesh Proppant Volume (lbm)	40/70-mesh Proppant Volume (lbm)	Pump Time (hrs)	Comments
16A(78)-32	Stage 4 (16A)	1	Slickwater	4,000	35	54,600	79,800	2.5	
16A(78)-32	Stage 5 (16A)	1	XL CMHPG	4,000	35	54,600	79,800	2.5	
16A(78)-32	Stage 6 (16A)	1	XL CMHPG	4,000	35	54,600	79,800	2.5	May include alternative proppants (TBD).
16A(78)-32	Stage 7 (16A)	4	XL CMHPG	16,000	80	218,400	319,200	4.0	Evaluate multiples clusters / Cluster spacing = 50 ft
16A(78)-32	Stage 8 (16A)	8	XL CMHPG	32,000	80	436,800	638,400	7.0	Evaluate multiples clusters / Cluster spacing = 25 ft
16A(78)-32	Stage 9 (16A)	8	Slickwater	32,000	80	436,800	638,400	7.0	Evaluate multiples clusters / Cluster spacing = 25 ft

In this study, we performed numerical simulations of the planned stimulation tests. Plans for long-term circulation between wells have not been finalized. Nevertheless, we extended the simulations to include long-term circulation and thermal drawdown. The simulations solely include the stimulations of Well 16A, and not the smaller-scale treatments planned for 16B. The simulations assume that if fractures from 16A intersect 16B, they will be able to connect to the nearest perforation cluster in the well.

The numerical models are based on simulations that were previously calibrated to the injection data and microseismic from Stage 3 of Well 16A (McClure, 2023a). After the upcoming stimulations have been performed in 16A, it will be relevant to compare model predictions against actual observations. In particular, DAS fiber measurements in 16B will quantify the number and timing of frac hits, and microseismic monitoring will suggest the overall size and shape of the region of stimulation. Circulation tests will measure the flow capacity of the system, and a spinner log will measure the uniformity of injection from Well 16A and production into Well 16B.

The model is calibrated to a single fracturing stag. There are few, if any, other field-scale datasets that might be appropriate for calibrating the simulator for these upcoming stimulations – plug and perf propped hydraulic fracturing from a sub-horizontal well in a granitic formation. Thus, we do not expect 'perfect' model predictions. Another round of model calibration will be performed once the new data have been acquired.

In addition to the 'Base Case' simulation, a variety of sensitivity analysis simulations were performed. These simulations explore the effect of uncertain model parameters (such as fracture toughness) and explore alternative operational scenarios (such as circulating CO_2 instead of water).

2. METHODS

2.1 Conceptual model for fracture geometry and stimulation mechanism

Historically, EGS modeling has been challenged by lack of clarity on the appropriate choice of modeling assumptions. Through the 1980s to 2000s, the initiation and propagation of newly forming fractures during stimulation was largely neglected in numerical modeling codes for EGS stimulation and circulation (see review by McClure et al., 2014a). In the past decade, it has become common to include newly propagating hydraulic fractures in EGS simulations. This shift has been driven by: (a) a reevaluation of historic data, which consistently indicates injection pressure reaching the minimum principal stress and exhibiting pressure-limiting behavior (McClure and Horne, 2014a); (b) field data collection, such as at the EGS Collab, Desert Peak, and recently at the FORGE project, where injection slightly below the magnitude of Shmin has shown shear stimulation to be ineffective (Chabora et al., 2012; McClure and Horne, 2014b; Fu et al., 2022; Lawrence Berkeley Laboratory, 2023; McLennan et al., 2023); and (c) the recognition that EGS designs relying on shear stimulation have not consistently achieved adequate reservoir performance.

Shear stimulation appears to be the dominant mechanism when injecting into large, preexisting fault zones (Evans et al., 2005). However, in the absence of such features, propagation of newly forming fractures appears to be the dominant mechanism. Even in the presence of natural fractures optimally oriented to slip, shear stimulation can be unsuccessful if: (a) fracture have cohesive strength that prevents slip, (b) shear stimulated natural fractures are not large and pervasive enough to create percolating, continuous flow pathways, or (c) slip does not result in sufficient increase in conductivity.

Among the newer generation of EGS stimulation models that include propagation of hydraulic fractures, there is lack of consensus about whether to use a model based on a 'discrete fracture network' (DFN) of preexisting fractures. This lack of consensus mirrors – and perhaps lags – the evolution of thinking that has occurred in the shale industry regarding hydraulic fracture geometry. In the early 2010s, DFN modeling of stimulation was widely-adopted in the shale industry. However, since then, DFN modeling has become much less common. This transition has coincided with a shift from relying primarily on microseismic clouds to relying on higher fidelity observations taken directly at the wellbore, such as DAS strain measurements and, sometimes, core-through analysis. Microseismic signatures lack the resolution to differentiate the details of fracture geometry and stimulation mechanism. DAS strain measurements in offset wells can measure individual frac hit locations and orientations, along with the strain field associated with fracture deformation. Core-through provides even more granular information about fracture morphology. The newer generation of data has demonstrated that fracture stimulation in shale is nearly always dominated by propagation of largely planar fracture features, oriented perpendicular to Shmin, with minimal lateral branching (Ugueto et al., 2019a, 2019b, 2021; Raterman et al., 2017, 2019; Gale et al., 2018, 2019; Maity and Ciezobka, 2020; Craig et al. 2021; Shahri et al. 2021). At small-scale, field-scale hydraulic fractures demonstrate complexities such as step-overs and propagation in multistranded swarms. However, at field-scale, their propagation direction and morphology appears to be largely planar.

A key characteristic of DFN-style fracturing models is that they assume hydraulic fractures will often terminate at preexisting fractures, creating a branching, volumetric network, where flow pathways traverse multiple fractures with a diversity of orientations (Weng et al., 2011). This conceptual model is inconsistent with the common observations from DAS and core-through in shale that show fractures propagating in narrow corridors, with relatively consistent orientation, and flow almost entirely localizing to newly forming fractures. The 'fracture termination' process can be reproduced in the lab, and undoubtedly occurs to some degree in-situ. However, field observations indicate that hydraulic fractures often have no trouble crossing preexisting fractures, and if they do terminate, they may experience no more than a brief 'jog' before reinitiating a short distance from the termination (Fu et al., 2022). Further, hydraulic fractures can 'propagate around' natural fractures (Bahorich et al., 2012), and even a small amount of patchy cementation along a natural fracture may permit a hydraulic fracture to 'break through,' even if there are other parts of the fracture that are uncemented and potentially capable of causing termination (Fu et al., 2016).

A 'planar fracturing' model that does not include a DFN does not implicitly assume that there are not any natural fractures. Instead, it assumes that the effect of natural fractures can be captured by adjusting the formation permeability and other formation properties in the matrix 'continuum' to account for the effect of natural fractures. More broadly, a DFN may only be justified if fractures are experiencing abundant termination and branching in a 'complex fracture network,' rather than localizing into largely planar opening model hydraulic fractures.

We do not yet have high-fidelity measurements of far-field fracture geometry in crystalline basement EGS projects. Notwithstanding the comments above, it is possible that – for crystalline basement lithology such as at FORGE – it will turn out that fracturing does create a volumetric, 'complex fracture network.' Fortunately, the FORGE project is in the process of gathering high fidelity measurements of far-field fracture geometry. When Well 16B was drilled, sections were cored through the regions of rock associated with the first three stages of stimulation in 16A, where intersecting fractures were created and/or reactivated by injection. The results from the core-through are being analyzed and have not yet been published. When the upcoming stimulation stages are performed in 16A, fiber in 16B will measure the number, orientation, and location of the offset frac hits. The strain field measured in the 16B fiber will make it possible to differentiate between opening mode hydraulic fractures and shearing preexisting fractures (Ugueto et al., 2023; Ratnayake and Ghassemi, 2023).

In recent modeling at the FORGE project, different conceptual models have been used. Xing et al. (2023) used a very dense DFN (100s of preexisting fractures). Podgorney et al. (2023) used an intermediate density DFN (10s of preexisting fractures). Ghassemi and Kumar (2023) used a low density DFN (around ten preexisting fractures). McClure (2023) used solely a 'planar fracture modeling' approach without any preexisting discrete fractures.

For the present work, we adopt the 'planar fracture modeling' approach. Future data collection will significantly reduce uncertainty about stimulation mechanism and provide an opportunity to compare against modeling predictions.

2.2 Numerical modeling approach

The simulations were performed with a fully integrated, three-dimensional hydraulic fracturing, wellbore, and reservoir simulator (McClure et al., 2023). Quoting from McClure et al. (2022):

> "Hydraulic fractures are represented discretely with planar elements; the well(s) are represented with linear elements; and the matrix is represented by volumetric elements using a rectilinear grid. The matrix mesh is non-conforming to the fracture elements; a submeshing technique is used to achieve numerical accuracy, even if the matrix mesh is coarse relative to the radius of investigation. In each timestep, the simulator enforces a set of balance equations: mass balance on fluid components, proppant types, and water solutes; energy balance; and (in the wellbore) momentum balance. In addition, the simulator solves the equations of linear elastic continuum mechanics to calculate the stress changes caused by fracture opening and by pressure and temperature changes in the matrix. All equations are solved simultaneously in every element in every timestep.
>
> …

Fracture propagation is described with linear elastic fracture mechanics. A newly developed method called MuLTipEl is used to track the position of the crack tip within 'tip' elements, giving the algorithm the resolution to handle propagation across layers much thinner than the element size (Dontsov et al., 2022).

The contact problem of fracture opening and closure is particularly challenging. A crack is mechanically 'open' when the fluid pressure exceeds the normal stress. The walls come out of contact, and the simulator enforces the boundary condition that the fluid pressure must be equal to the normal stress. The opening of a crack element impacts the stress of every other element, and so the entire system of crack apertures and induced stresses must be solved simultaneously in all elements, along with being solved simultaneously with all other equations in the system, such as fluid mass balance. When the cracks walls are in contact, the aperture is nonlinear function of effective normal stress and the amount of proppant present in the element. The constitutive equations for transport are different in mechanically open and closed cracks (and also, are affected by whether or not proppant is present in the fracture), and so the simulator uses a specially designed set of constitutive equations to smoothly transition between these different constitutive equations as elements open and close."

Water properties are calculated from IAPWS correlations (Cooper, 2007). Density and phase behavior of non-water components (such as CO_2) are calculated with the Peng-Robinson equation of state. The CO_2 enthalpy is calculated with a Shomate correlation for the 'ideal gas' enthalpy, and then a 'real gas' adjustment with the Peng-Robinson equation of state. CO_2 viscosity is calculated using the Lohrenz-Bray-Clark (LBC) correlation.

Thermoelastic and poroelastic stress effects can be turned on or off in the simulator. When 'turned on,' they are calculated with a full 3D solution to the continuum mechanics equations, using zero displacement boundary conditions along the edges of the model.

2.3 Model parameters used in this study

The simulation parameters are similar to the settings that were used when matching to the 16A Stage 3 data, as presented by McClure (2023a). Table 2 summarizes the model parameters. Each stage was simulated according to the injection schedule in Table 1. The simulations do not include proppantless stimulations that have been performed previously (Stages 1-3).

Table 2: Parameters used in the Base Case simulation.

Permeability (assumed isotropic)	1 microdarcy	Formation compressibility	1e-5 psi^{-1}
Porosity	1%	Fracture gradient	0.73 psi/ft
Rock density	156 lb/ft^3	Rock heat capacity	0.239 BTU/(lb-R)
Thermal conductivity	1.445 BTU/(hr-ft-R)	Coefficient of linear expansion	5.56e-6 F^{-1}
Biot coefficient	0.35	Horizontal fracture toughness	2740 psi-in$^{1/2}$
Pore pressure gradient	0.41 psi/ft	Young's modulus	8e6 psi
Poisson's ratio	0.26	Surface temperature	68°F
Thermal gradient	0.033 F/ft	Crosslinked gel viscosity	70 cp at 170 s^{-1} and reservoir temperature
Crosslinked gel decay rate constant	0.67 hours^{-1}	Proppant grain diameter	100 mesh followed by 40/70 mesh
W_{fac} (adjustment to the effective aperture for conductivity)	0.395	$K_{Ic,fac}$ (scaling of toughness with sqrt fracture size)	0.1
k_{PDP} (effective permeability to leakoff)	55 microdarcy	$C_{open,fac}$ (reduction factor for vertical conductivity during propagation.	0.6

The wells are meshed to the surface, including both the vertical and inclined sections of the wells. The matrix and wellbore meshes are shown in Figure 1. The initial distributions of pore pressure, Shmin, and temperature are shown in Figure 2. The fractures are assumed to propagate perpendicular to Shmin. In reality, they may turn slightly due to stress shadowing, but this effect is expected to be minor (this assumption will be tested by DAS measurements in the 16B).

During circulation, injection is performed from Well 16A upward to Well 16B. The BHP of Well 16A is assumed to be 5387 psi, and the BHP in Well 16B is assumed to be 4240 psi. The injection temperature is conservatively estimated to be low, 65°F.

The simulator is capable of including the well in the model during circulation and specifying wellhead boundary conditions, but for simplicity, the simulations in this study used bottomhole boundary conditions during circulation (in contrast, wellhead boundary conditions were used during fracturing). The BHP values are assigned at the toes of the wells and hydrostatically adjusted for fracture connections uphole. The BHP assumptions are relatively conservative, especially at the production well, where it is implicitly assumed that the well is not pumped, and a modest backpressure is held at the wellhead.
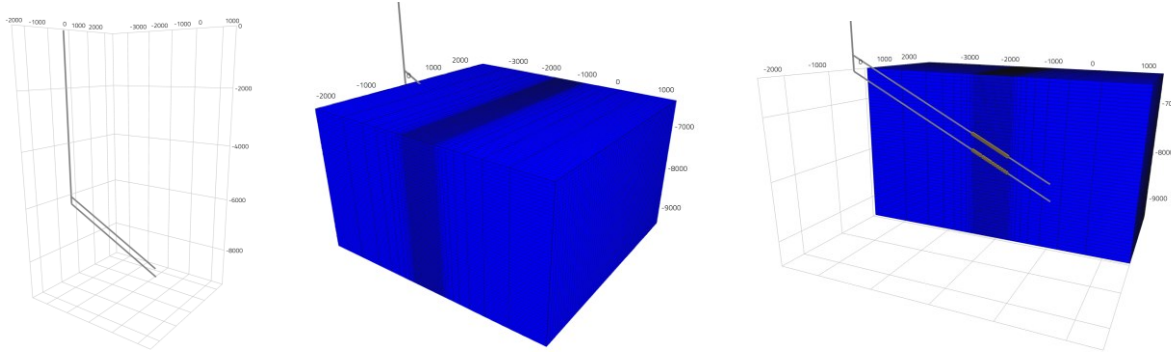
Figure 1: The wellbore geometries (left), the matrix mesh (middle), and the location of the perforations for Stages 4-9 (right).
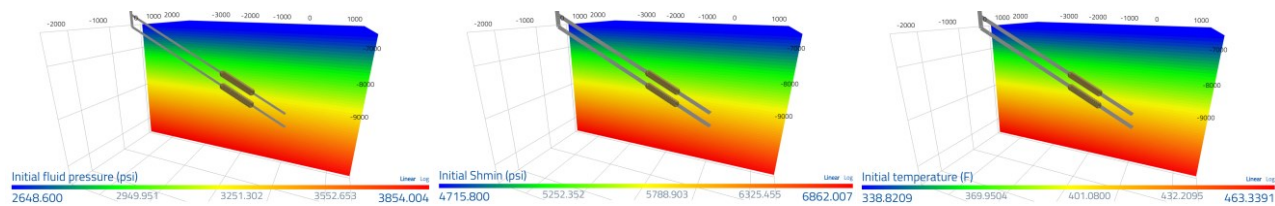

Figure 2: The initial pore pressure, stress, and temperature in the model.

A variety of sensitivity simulations were performed to explore the effect of uncertainty on the model and investigate alternative operational scenarios. Each sensitivity changed one parameter at a time to determine the effect of that parameter on model outcomes. For each sensitivity that was investigated, the changes that were made relative to the Base Case are summarized in Table 3.

Table 3: Differences between the Base Case simulation and the sensitivity analysis simulations.

Sensitivity	Changes made relative to Base Case	Base Case Value
1. Low toughness	Horizontal = vertical = 500 psi-in$^{1/2}$	Horizontal = 2740 psi-in$^{1/2}$, Vertical = 4510 psi-in$^{1/2}$
2. Low Conductivity During Propagation	Low, 'effective fracture aperture conductivity factor' = 0.2	Moderate, 'effective fracture aperture conductivity factor' = 0.4
3. Thermoelasticity	Thermoelasticity included	Thermoelasticity not included
4. Inflow control with Thermoelasticity	1 x 0.08" diameter perforation every 30 ft along Well 16B	4 x 0.4" perforations located at each fracture intersection
5. CO_2 Injection	Inject CO_2 during production	Inject water during production

3. RESULTS AND DISCUSSION

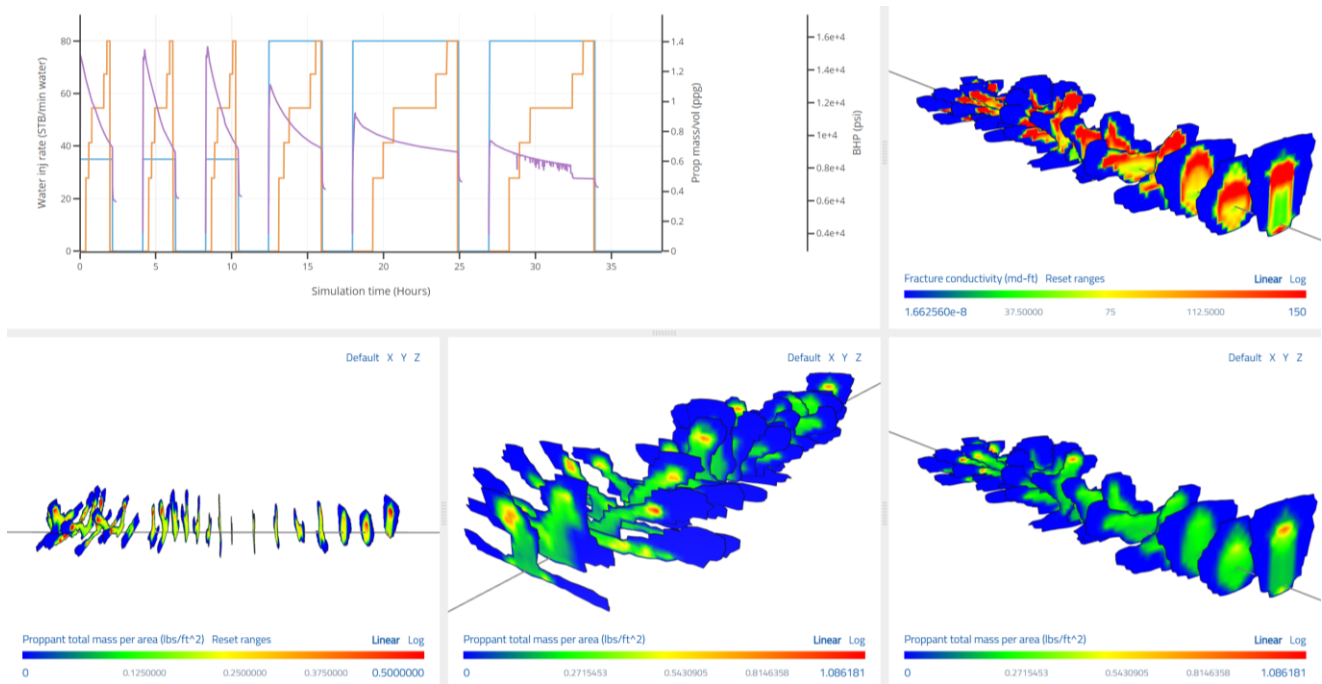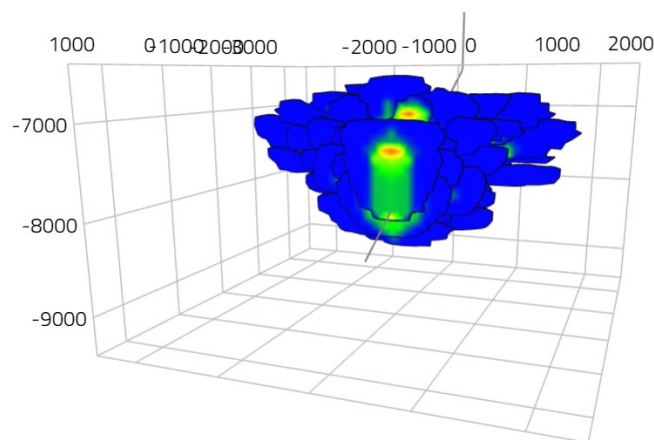### 3.1 Base Case

3.1.1 Overall fracture geometry

Figure 3 and Figure 4 show the fracture geometries from the Base Case simulation. The earlier stages, which use greater cluster spacing, have relatively rounded and symmetrical fractures. The later stages – which use spacing as tight as 25 ft – experience significantly greater fracture-to-fracture stress shadowing, and consequently exhibit more irregular geometry. Figure 5 shows the distribution of the stress shadow caused by fracture propagation prior to the second, fourth, and sixth stages (i.e., Stages 4, 6, and 8 overall). The stress shadow

builds up significantly as the stages progress. This occurs because of: (a) the accumulation of stress shadow from the prior stages, (b) the tightening cluster spacing in the later stages, and (c) the greater total fluid volume injected in the later stages.

In aggregate, the fractures created around the wells have a maximum predicted half-length of 2,000 ft and a maximum height of 1,850 ft. However, individual fractures have considerably smaller geometry. For example, the fracture from the first stage (i.e., Stage 4 overall) has a height of 1,100 ft, and a half-length of 550 ft. Proppant extends laterally as far as 1,200 ft from the well, and vertically as far as 1,100 ft above the well. But again, the propped dimensions of individual fractures have significant variability within these ranges. For example, the fracture from Stage 4 has a propped height of 850 ft and propped half-length of 265 ft.

Figure 3: Results from the Base Case simulation at the start of circulation between the wells. The image is stretched 15x in the direction perpendicular to Shmin. The toe of the well is located towards the right-side of the figures. The panels on the bottom show the fracture geometries from three different camera angles.


Figure 4: Fracture geometry from the Base Case simulation.
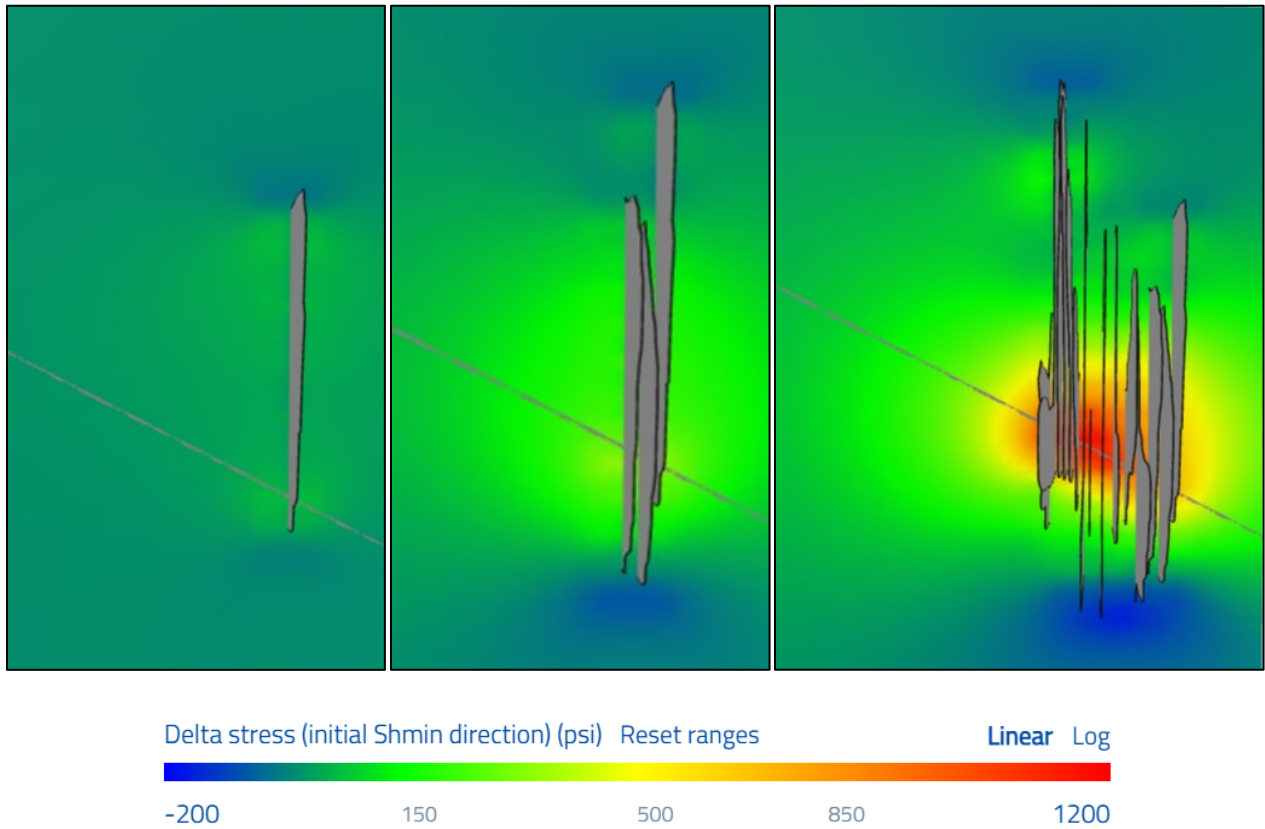
Figure 5: Distribution of stress shadow around the fractures propagating during the base case simulation.

3.1.2 Propped geometry

Back-of-the-envelope calculations confirm that propped heights of 850 ft are not unreasonable. Figure 6 shows various fracture properties during injection into the first stage (Stage 4 overall). For 100 mesh proppant in slickwater (with a viscosity around 0.6 cp at low shear rate, taking into account the effect of both temperature and the viscosity-increasing non-Newtonian friction reducer), the settling rate is around 0.078 ft/s at dilute proppant concentration and around 0.02 ft/s at higher proppant concentration (the difference is due to 'hindered settling' at higher concentration). For more details on the proppant settling calculations implemented in the simulations, refer to Section 8 from McClure et al. (2023). The fracture aperture above the well is around 0.12 inches, and the fluid velocity upward is 0.5-0.75 ft/s (equivalent to around 0.01-0.015 ft^3/s per cross-sectional length). Because the upward velocity is much greater than the settling rate, the proppant is carried upward to significant height. After closure, settling is reduced by the 'proppant trapping' mechanism that accounts for fracture roughness (up to a maximum of 0.15 lb/ft^2), and the fracture closes within 10s of minutes after shut-in (due to the relatively high leakoff permeability, as discussed by McClure, 2023a).
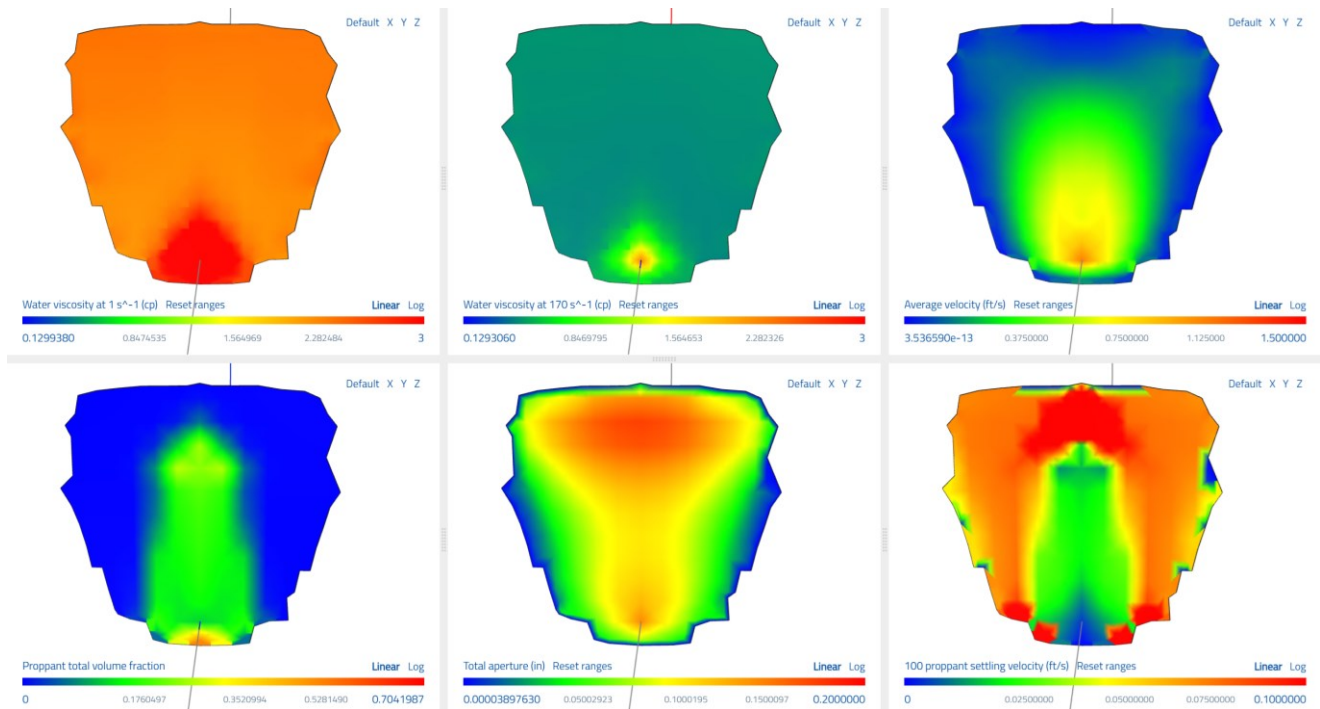
Figure 6: Distribution of fluid viscosity, flow velocity, aperture, proppant volume fraction, and proppant settling velocity during the first stage (Stage 4 overall).

3.1.3 Long-term circulation – flow rates, fracture conductivity, and fracture connections

Figure 7 shows results from long-term circulation in the Base Case simulation. The injection rate starts at around 2 bpm (2,880 STB/day; 5.3 kg/s; 700 lbm/min) and declines gradually, reaching 1.4 bpm (2016 STB/day; 3.7 kg/s; 490 lbm/min) at the end of 20 years. The production rate starts at around 1.2 bpm (1,728 STB/day; 3.2 kg/s; 420 lbm/min) and increases to around 1.4 bpm (2,016 STB/day; 3.7 kg/s; 490 lbm/min).

The target flow rate for an economically successful EGS doublet is at least 54,250 STB/day (100 kg/s; 13,200 lbm/min). The projected flow rate for the 16A/16B doublet falls far short of this target. This result is not unexpected because the FORGE wellbores are designed for research purposes and are not full-scale EGS systems. A full-scale system may have a lateral length of 6,000 ft or more, with perforation clusters roughly every 25 ft. This implies several 100 fracture connections between the wells. The 16A design includes only 23 perforation clusters. If 75% of these result in a connection, we should expect around 17 fracture connections, an order of magnitude less than a full-scale system. Furthermore, in a full-scale system, an array of wells would allow injection/production in both directions, improving flow capacity and recoverable heat per well. Finally, the BHP conditions between the injection and production wells in the simulations are conservative – applying only 1,147 psi of pressure difference between the wells. More aggressive pumping or injection could increase that pressure difference by a factor of 50% or more, depending on conditions.

At the end of 20 years, the difference between the injection and production volumes in the Base Case simulation is around 2 million STB, around 13% of the total injection. This number is likely an underestimate, because the simulation mesh used 'no-flow' boundary conditions on its edges. With a much larger (effectively infinite) simulation mesh, there would have likely been even more net injection. On the other hand, the fluid loss in this flow configuration is not representative of the behavior of a 'full-scale' EGS system. With stimulation of full laterals (rather than only a section of the laterals), the 'outer perimeter' of the system (from which leakoff occurs into the far-field) would comprise a much smaller fraction of the total system. Furthermore, with an array of wells (rather than simply a doublet), injection wells could be more completely surrounded by production wells (indeed, systems would likely be designed with production wells along the 'outer perimeter' of the well configuration, with the injection wells inside). With these design changes in a full-scale system, fluid loss would be significantly reduced.

The system permeability has a strong effect on far-field fluid loss. The model permeability is 1 microdarcy, which is reasonable, considering the observations at FORGE, but which is considerably higher than the expected permeability of unfractured granitic rock. Probably, natural fracture permeability contributes to far-field fluid loss at FORGE, which elevates the system permeability.

The flow rate through the system is determined by the fracture conductivity and the number of fracture connections between the wells. As a model assumption, the unpropped conductivity is low, and so flow rate is mainly determined by the propped conductivity. In turn, this is determined by the amount of proppant placed in each fracture element (in the range of 0.15-0.5 lb/ft^2 in most of the propped area), and the proppant pack conductivity permeability. The proppant pack conductivity is a function of effective normal stress. The assumed

relationship between conductivity, proppant concentration, and effective normal stress is an important modeling uncertainty. In the future, when circulation is performed between 16A and 16B, we will have the opportunity to empirically measure the fracture conductivity and compare with the model assumptions.

In the authors' opinion, the parameters used in this study are reasonable, considering experience from recent EGS projects (Norbeck and Latimer, 2023). The propped fracture conductivities in the model are in the range of 30-150 md-ft (Figure 7). These values are consistent with observations from well-to-well interference tests performed when wells are first put on production. For example, Table 4 from Almasoodi et al. (2023) shows conductivity estimates of 45-135 md-ft measured between shale wells at a lateral spacing of 1,000 ft. In an even more relevant example, Titov et al. (2024) use interference test analysis to estimate conductivity between propped EGS wells as part of Fervo Energy's Project Red and estimate values between 68.1 and 163.8 md-ft.

In shale, interference tests show that when wells have been producing for an extended period, propped conductivity decreases by roughly an order of magnitude, relative to when they are first put on production. However, this observation is not analogous to the expected behavior during EGS circulation. In shale, long-term production is accompanied by pervasive pressure depletion throughout the reservoir (causing a large increase in the effective normal stress on the fractures, up to 8,000 psi or more, depending on the formation). In EGS, pressure is permanently supported by one or more injection wells. Further, as discussed in Section 3.4, thermal stresses will cause destressing and a *reduction* in effective normal stress over time.

Table 4 shows the number of frac hits on Well 16B associated with each stage in Well 16A, along with the percentage of perforation clusters resulting in a frac hit. The three stages with a single cluster each result in a frac hit, corresponding to 100% efficiency. The stages with four clusters (50 ft spacing with X-link) and eight clusters (25 ft spacing with X-link) have 75% frac hit efficiency. The final stage – eight clusters (25 ft spacing with slickwater) – has only 37% frac hit efficiency, even though all clusters generate a significantly-sized fracture. Because of the fracture-to-fracture stress shadowing, the fractures in the final stage are forced to propagate 'out of each other's way,' which results in irregular, relatively non-overlapping geometries, and fewer fractures that propagate directly upward.

When the actual stimulations are performed, the cemented fiber in 16B will be able to directly observe individual frac hits. It will be very valuable to compare the observed frac hit counts with the model predictions. As shown in Sections 3.2 and 3.3 below, moderately different model assumptions would have resulted in more optimistic predictions for frac hit efficiency in Stage 9. The model parameters in the Base Case model are drawn from calibration to only a single fracturing stage – Stage 3 from the previous Well 16A treatment – and it is possible that further data will lead to adjustments in the 'best fit' model parameters. Either way, the field observations will be extremely valuable for model calibration and validation.
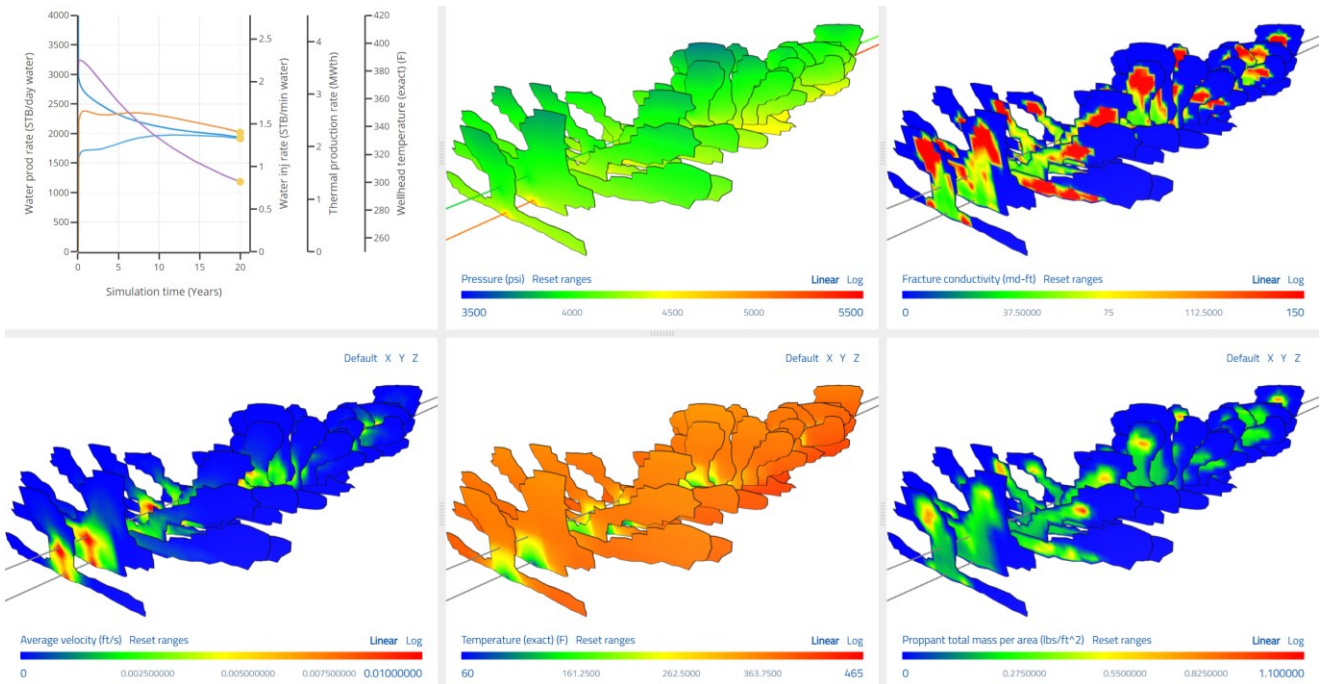
Figure 7: Results from the Base Case simulation at the end of 20 years of circulation between the wells. The image is stretched 15x in the direction perpendicular to Shmin. The toe of the well is located towards the right-side of the figures. On the line plot, purple is produced temperature, orange is thermal production rate, dark blue is water injection rate, and light blue is water production rate.

Table 4: Number and percentage of frac hits at Well 16B for each stage in the Base Case simulation.

Stage	# clusters @ cluster sp (ft)	% frac connection
Stage 4	1 @ 50ft	100%
Stage 5	1 @ 50ft	100%
Stage 6	1 @ 50ft	100%
Stage 7	4 @ 50ft	75% (3 hits / 200 ft)
Stage 8	8 @ 25ft	75% (6 hits / 200 ft)
Stage 9	8 @ 25ft	37% (3 hits / 200 ft)

3.1.4 Long-term circulation – thermal drawdown

Figure 7 shows that over 20 years, the produced temperature drops from 388°F to 300°F. As shown in Figure 8, the distribution of flow between the fractures is relatively uniform, with a roughly 2-3x difference between the highest flowing fracture and lowest flowing fracture. The relatively uniform flow distribution was beneficial for thermal longevity. The right panel of Figure 8 shows that the density of thermal drawdown is greatest in the later stages, which is where the cluster spacing is tighter.

In Section 3.4, the Base Case simulation is repeated with thermoelastic stresses activated. The thermal drawdown and reservoir characteristics are substantially different.
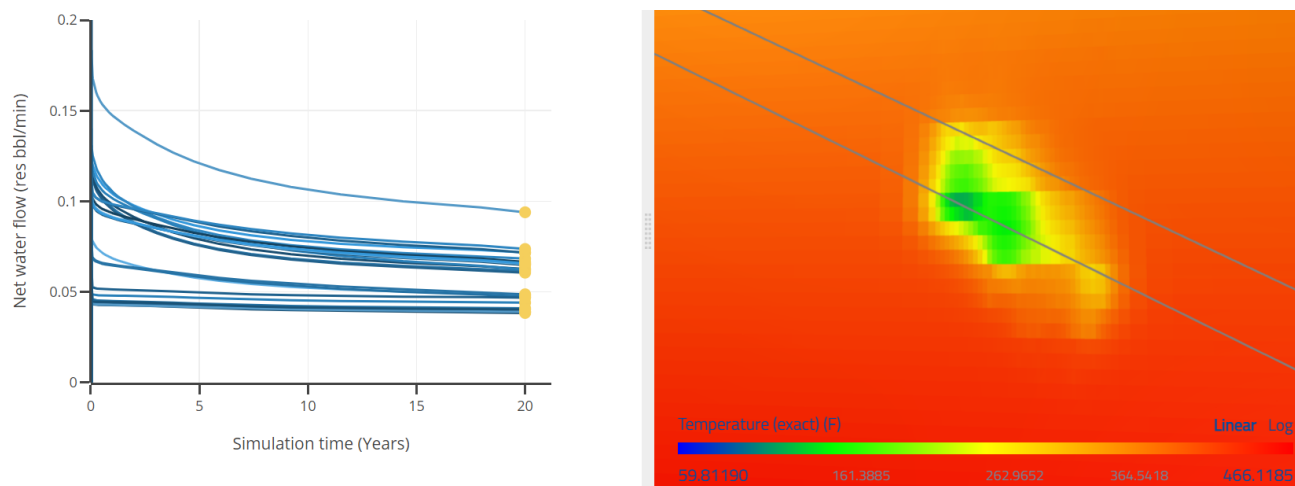
Figure 8: Flow rate per fracture versus time (left) and the temperature distribution in a vertical cross-section through the formation after 20 years of circulation (right) from the Base Case simulation.

3.2 Lower Toughness

Figure 9 shows the fracture geometries from the Lower Toughness simulation. The lower toughness results in greater fracture surface area and weaker stress shadowing. As a result, the fracture geometries are more uniform, and the frac hit efficiency is higher than in the Base Case simulation. All but one of the perforation clusters in Well 16A achieves a connection with Well 16B (22 out of 23).
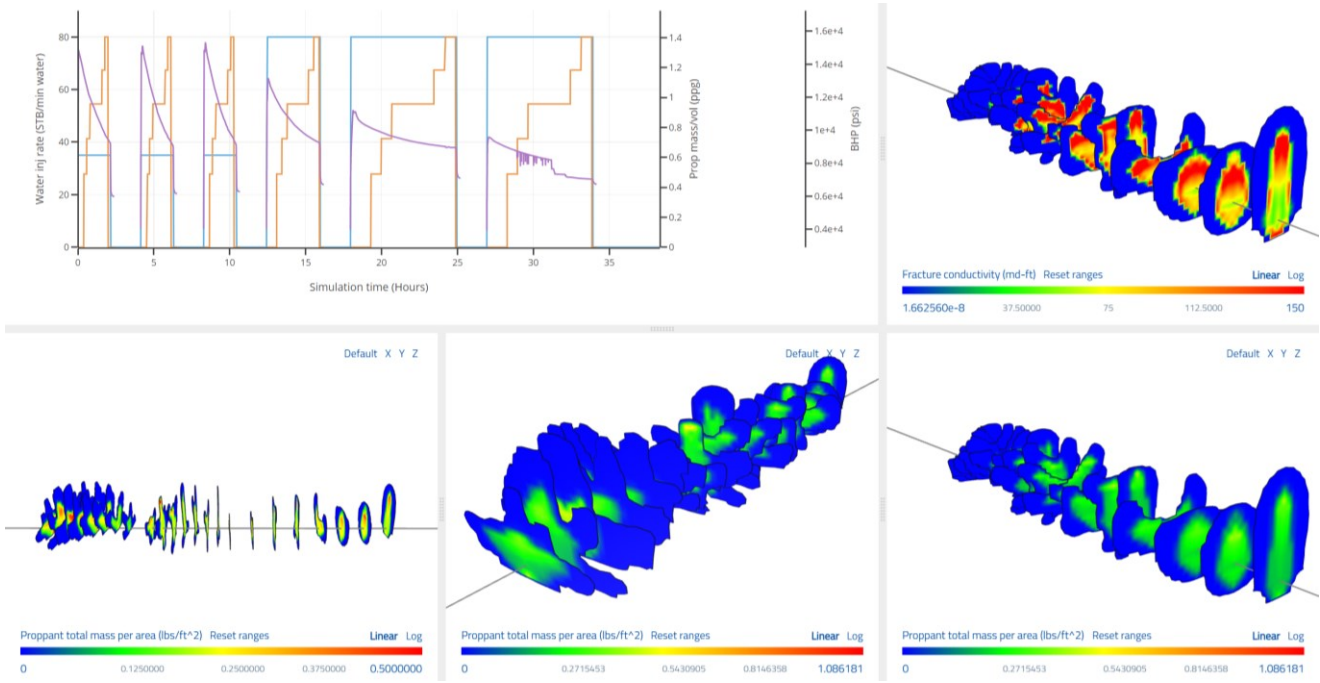
Figure 9: Results from the Lower Toughness simulation at the start of circulation between the wells. The image is stretched 15x in the direction perpendicular to Shmin. The toe of the well is located towards the right-side of the figures. The panels on the bottom show the fracture geometries from three different camera angles.

3.3 Lower Conductivity During Propagation

Figure 10 shows results from the Lower Conductivity During Propagation simulation. With lower conductivity, there is greater pressure gradient from wells to the fracture tips, which reduces the effect of stress shadowing and regularizes the fracture geometries (Dontsov and Suarez-Rivera, 2020). This behavior is somewhat analogous to the effect of lower toughness, except that it results in slightly smaller fractures, when compared with the Base Case simulation. This simulation has significantly better frac hit efficiency during the final stage, compared with the Base Case simulation (100% instead of 37%), and slightly lower efficiency in the penultimate stage (five hits instead of six).
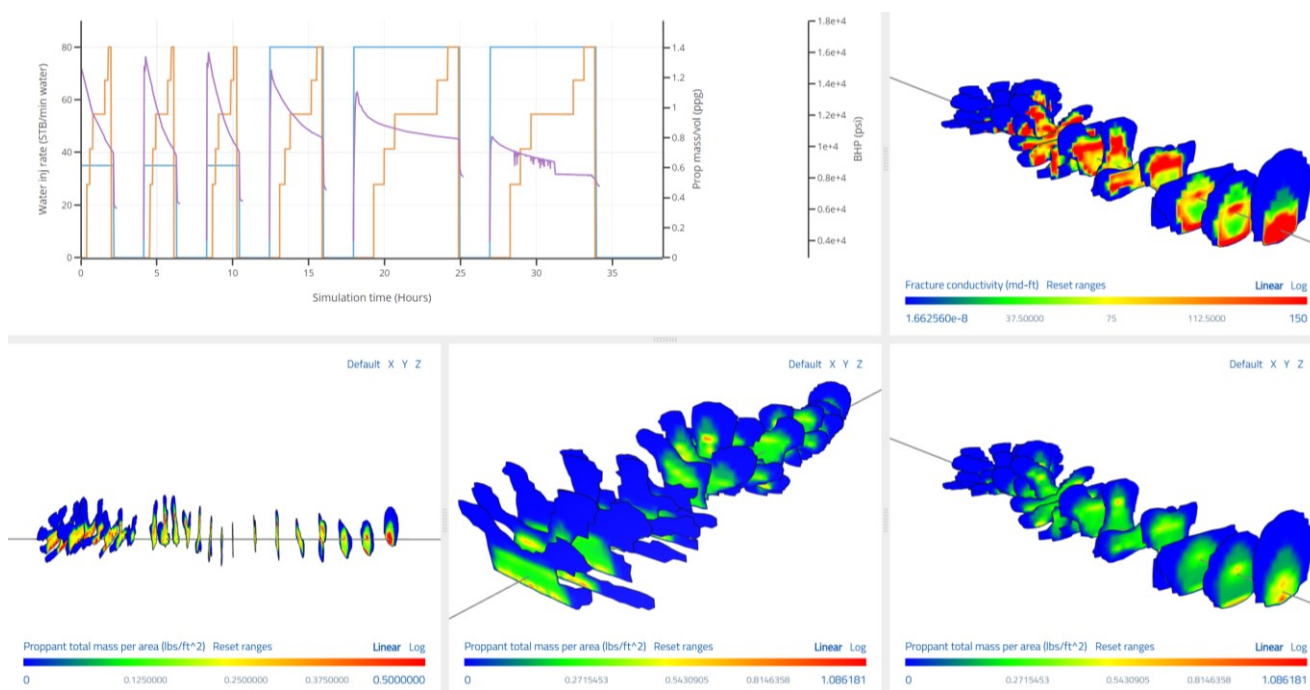
Figure 10: Results from the Lower Conductivity During Propagation simulation at the start of circulation between the wells. The image is stretched 15x in the direction perpendicular to Shmin. The toe of the well is located towards the right-side of the figures. The panels on the bottom show the fracture geometries from three different camera angles.

3.4 Thermoelasticity

Figure 11 shows circulation results from the Thermoelasticity simulation. Thermal breakthrough occurs within 0.6 years, and so the simulation is only performed for two years, ending once the produced temperature falls below 200°F.

Thermoelasticity significantly affects system behavior. Cooling induces stresses of 1,000s of psi, which results in fracture reopening, with maximum apertures predicted to exceed 1.5 inches. This is a very large aperture, and in reality, the tensile strain may be accommodated across multiple fractures and a much more complex geometry than represented in the planar fracture model. As the fractures mechanically open, their conductivity increases by orders of magnitude. Some of the proppant settles to the bottom, and some remains 'trapped' according to the fracture trapping mechanism built into the simulator. In the short term, the fracture opening is beneficial for power production because it increases the circulation rate. During the first 6 months of circulation, the predicted production rate reaches the specified maximum allowed rate of 5,000 STB/day (roughly 2x higher than the Base Case simulation), despite maintaining a production well BHP greater than the specified minimum (i.e., utilizing less ΔP to drive flow than permitted by the specified BHP conditions). After about 7 months, the produced temperature falls off sharply as the 'fracture opening' front of one of the fractures reaches the production well, creating a short-circuit pathway that allows cool fluid to flow through, bypassing the heat in place.

Is this a realistic simulation prediction? It is unclear. On the one hand, we can be confident that contraction will induce cooling in the rock mass, and this has potential to open fracture flow pathways. On the other hand, the details of the process are more complex than represented in the simulation. For example, calculations suggest that fractures should begin opening in the direction perpendicular to SHmax (Tarasovs and Ghassemi, 2010), a process that is not captured in the simulations. A fracture simulation approach that permits more general representation of fracture geometry, such as phase field (Fei et al., 2023), would be needed to fully capture 3D fracture geometries arising from these thermal cooling effects.

In the future, circulation tests will be performed at FORGE, and it will be possible to evaluate if the observed behavior is more similar to the Base Case simulation or the Thermoelasticity simulation. Effects from thermoelastic coupling to fracture conductivity should be evident within relatively short timescales. For example, the Thermoelasticity simulation predicts sharply rising injectivity/productivity over the first 6 months of circulation. In addition, there may be diagnostics that provide confirmation of thermoelastic opening (for example, time-lapse tracer tests). Spinner logs may be used to assess whether flow is becoming more uneven over time.

In this FORGE simulation, the nonuniformity of the fracture spacing probably contributes to early breakthrough. Because some fractures are spaced tighter than others (due to variable cluster spacing), there is uneven tendency for cooling and thermal opening. A commercial project would almost certainly use uniform cluster spacing.

Despite the uncertainty in the simulation predictions from the Thermoelasticity simulation, it is clear that technologies to ensure flow-conformance are a high priority for future EGS research and development.
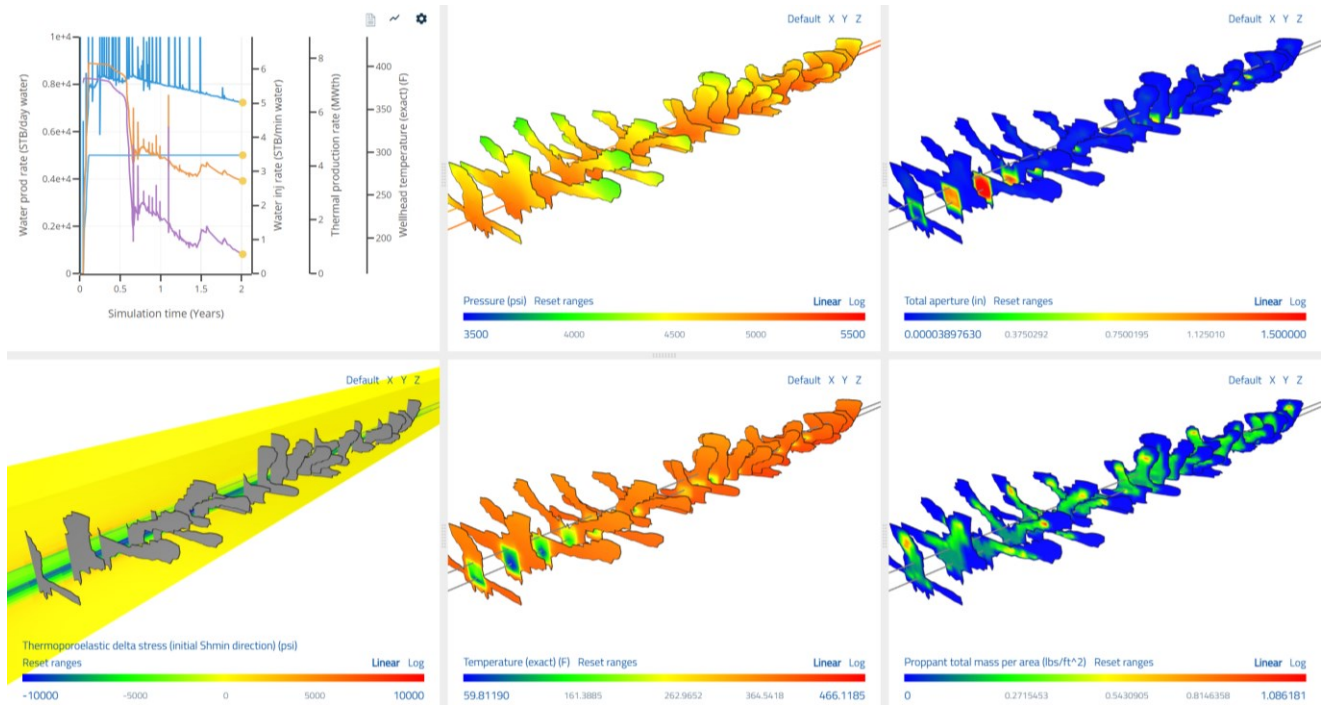
Figure 11: Results from the Thermoelasticity simulation at the start of circulation between the wells. The image is stretched 30x (instead of 15x) in the direction perpendicular to Shmin. The toe of the well is located towards the right-side of the figures. On the line plot, purple is produced temperature, orange is thermal production rate, dark blue is water injection rate, and light blue is water production rate.
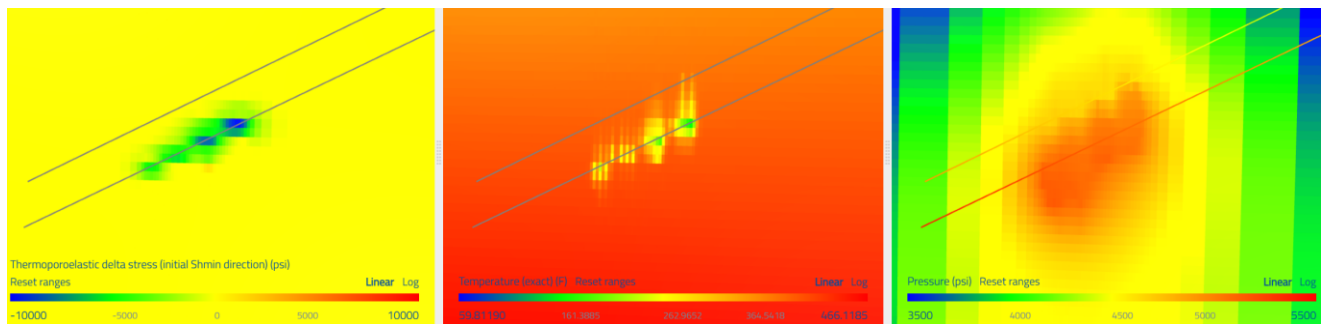
Figure 12: The distribution of temperature, stress change, and pore pressure in the Thermoelasticity simulation shortly before the onset of thermal breakthrough a seven months. The toe of the well is located towards the left-side of the figure.

3.5 Inflow Control with Thermoelasticity

Figure 13 shows the results from a simulation with thermoelasticity and inflow control. The inflow control is modeled as a single, small hole in the casing at regular intervals along the production well, 16B. Because the hole diameter is so small, flow into any single orifice is throttled, and limited from being excessive (see McClure 2023b, for more discussion of this topic).

Fracture opening extends continuously between the injection and production wells, creating the potential for short-circuit pathways. However, the inflow control prevents excessive flow rate or localization along these pathways. The thermoelastic cooling causes a gradual increase in production rate over time but does not cause premature breakthrough.

The right panel of Figure 14 shows the vertical volumetric flow rate per cross-sectional area within some of the thermoelastically opened fractures. Because they are effectively infinite conductivity, the density difference between the cool injected fluid and the hot formation

is able to drive buoyant convection – with downward flow from the injection well and circulation back up on either side. This process improves the heat sweep efficiency and causes gradual downward propagation of the fractures, accessing additional surface area, and delaying thermal decline. This mechanism is discussed in detail by McClure (2023b).

Flow conformance in EGS could be improved through a variety of mechanisms, and this is an area of active research. The simplest approach would be remedial – wait until a breakthrough has occurred, and then pump a cement squeeze into the offending wellbore interval. However, it would be better to prevent excessive localization from ever occurring at all. Aside from inflow/outflow control devices at the wellbore, another promising option is to use tracers or other diverter-like materials to identify and seal off excessively cool or conductive pathways (Hawkins et al., 2023).

Produced temperature declines over time and drops below 300°F after seven years. The reduction in temperature is not caused by 'thermal short-circuiting' (which is prevented by the inflow control), but rather is caused by the relatively tight well spacing and flow rate per cluster.
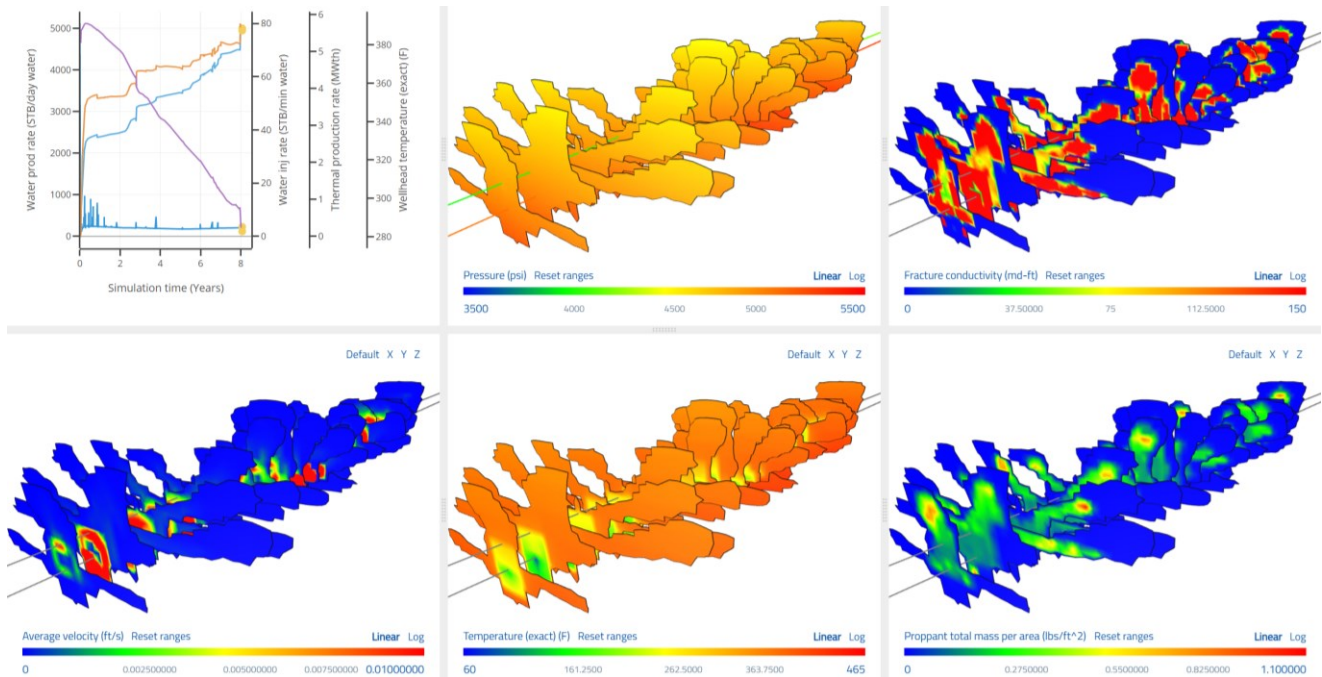

Figure 13: Results from the Inflow Control with Thermoelasticity simulation after 8 years of circulation between the wells. The image is stretched 15x in the direction perpendicular to Shmin. The toe of the well is located towards the right-side of the figures.
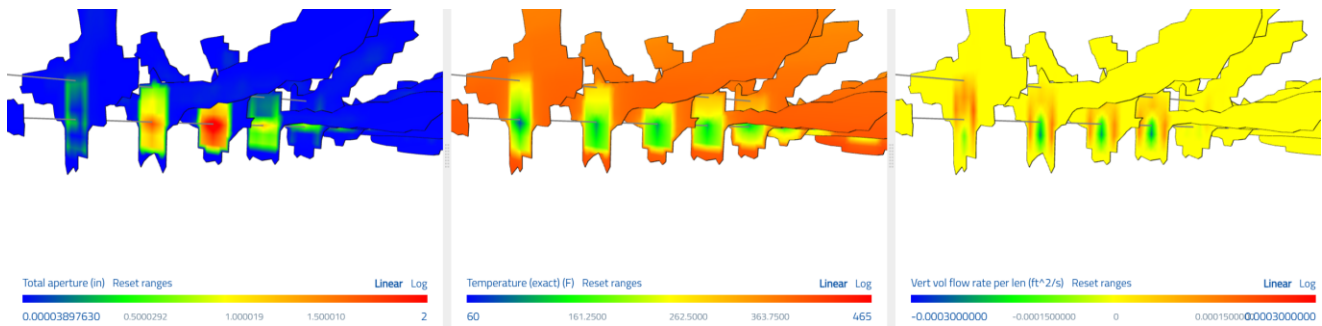

Figure 14: Results from the Inflow Control with Thermoelasticity simulation after 7 years of circulation between the wells. The image is stretched 30x in the direction perpendicular to Shmin. The toe of the well is located towards the right-side of the figures. The figures show opening due to thermoelastic stress reduction, and the development of buoyancy driven convection within the fractures.

3.6 CO2 Circulation

Figure 15 shows the results from the CO_2 Circulation simulation. The CO2 production rate is around 20,000 Mscf/day (16,000 lbm/min, or 12 kg/s). This is a significantly higher mass flow rate than achieved from circulating water in the Base Case simulation (which was around 4-5 kg/s). The viscosity of the CO_2 phase at reservoir temperature is around 0.03 cp, around 5x lower than the viscosity of water. The lower viscosity enables a much higher volumetric flow rate. However, the density of the CO_2 phase is lower, around 22 lb/ft^3 at reservoir conditions, compared with around 55.6 lb/ft^3 for water. The lower density of the CO_2 partially offsets the benefit of the lower viscosity.

CO_2 heat capacity and enthalpy are nonlinear functions of pressure and temperature. Overall, as it moves from the injection well to the production well (heating up and decreasing in pressure), the CO_2 gains as much as 184 BTU/lbm (428 kJ/kg). In comparison, circulating water gains as much as 318 BTU/lbm (740 kJ/kg). The relatively lower heat capacity of the CO_2 partially offsets the benefit from lower viscosity.

Overall, CO_2 circulation results in net thermal extraction in the range of 5.1 MWth, compared with net thermal extraction from circulating water in the Base Case simulation around 3.7 MWth.

Over the first seven years, the net injection of CO_2 is around 4 bcf (210,000 metric tons), around 10% of the cumulative injection volume. The rate of net injection gradually decreases over time, eventually going to near zero. However, this result is significantly affected by the no-flow boundary conditions on the edges of the model. With a larger problem domain, fluid loss would have been greater at late time. On the other hand, as discussed in Section 3.1.3, a full-scale system would have a significantly lower net fluid loss on a relative basis, because with longer laterals (more stages) and more wells, there would be fewer 'outer' fractures that can leak off fluid into the surrounding formation.

In a water-based system, net fluid loss to the formation is considered undesirable because it requires makeup water. However, in a CO_2 system, net injection may be considered beneficial and contribute to project economics through sequestration credits.

Depending on objectives, well configurations might be optimized to maximize or minimize net fluid loss to the formation. For example, the 'outside' wells in an array of wells could be selected to be either injectors or producers.
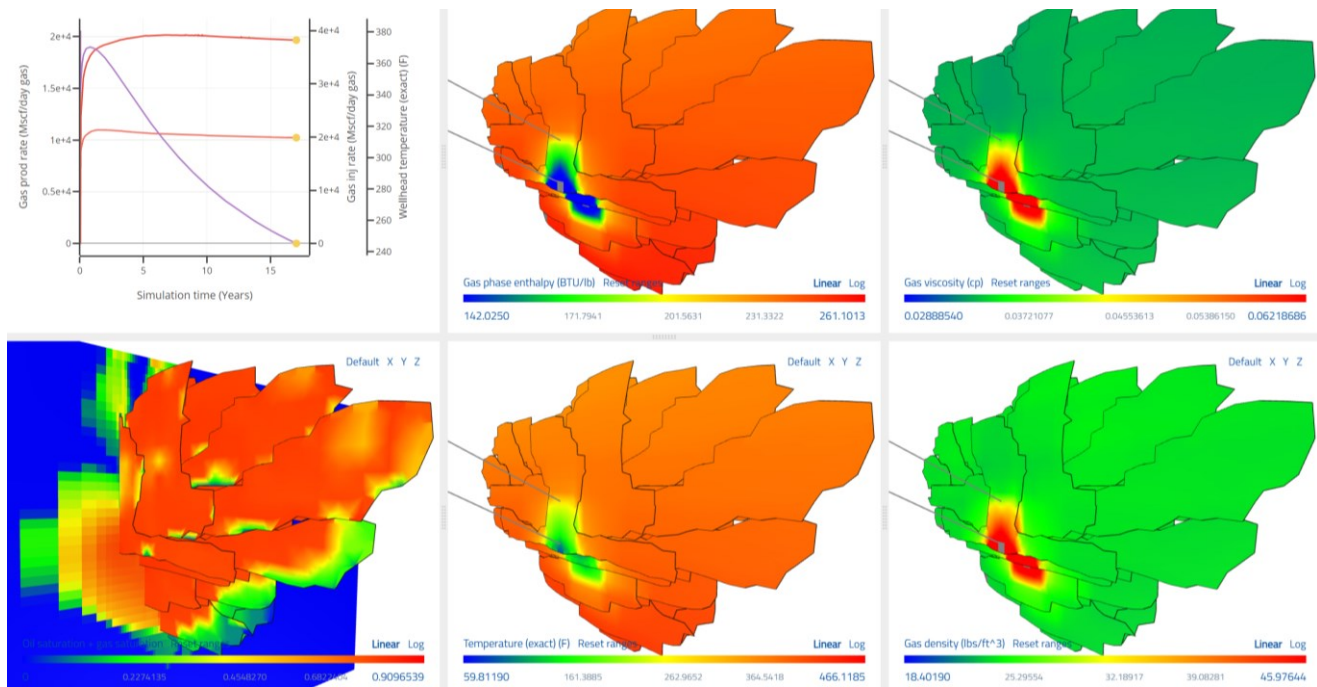
Figure 15: Results from the CO_2 Circulation simulation after two years of circulation between the wells. The toe of the well is located towards the right-side of the figures. The lower left panel shows the CO2 phase saturation.

4. CONCLUSIONS

The Base Case model makes specific, testable predictions regarding: (a) the number of frac hits that will be observed in the DAS fiber in Well 16B during the stimulation of Well 16A, (b) the overall size and shape of the fractured region that will be observed by microseismic signatures, (c) the flow rate and uniformity of flow that will be observed during circulation, and (d) the rate of thermal drawdown during long-term circulation. Regarding the rate of thermal drawdown, two different scenarios are presented, with and without thermoelastic

stress effects, providing different projections of performance. Future data collection will make it possible to test the model predictions and refine the model assumptions and parameters.

The modeling also considers two alternative scenarios: (a) thermoelasticity with inflow control, and (b) circulation with CO_2. The case with thermoelasticity and inflow control avoids the negative impact of thermoelasticity on long-term performance and receives a benefit from buoyantly driven convection and thermoelastically-driven downward fracture propagation over time. The case with CO_2 circulation achieves moderately higher overall rate of thermal extraction.

All the simulations in this paper are based on a 'planar fracture modeling' assumption that the dominant mode of fracture deformation and stimulation will be opening of largely continuous newly forming fractures perpendicular to Shmin (with the caveat that at small-scale, the fracture geometry is more complex than represented in the model, and likely multistranded). However, other conceptual models have been proposed for the stimulation mechanism at FORGE, and it has not yet been demonstrated conclusively which is most representative of reality. Future data collection at FORGE will help clarify these important modeling uncertainties.

REFERENCES

Almasoodi, Mouin, Thad Andrews, Curtis Johnston, Ankush Singh, and Mark McClure. 2023. A new method for interpreting well-to-well interference tests and quantifying the magnitude of production impact: Theory and applications in a multi-basin case study. Geomechanics and Geophysics for Geo-energy and Geo-resources 9(95).

Bahorich, B., J. E. Olson, and J. Holder. 2012. Examining the effect of cemented natural fractures on hydraulic fracture propagation in hydrostone block experiments. SPE-160197. Paper presented at the SPE Annual Technical Conference and Exhibition, San Antonio, TX.

Chabora, Ethan, Ezra Zemach, Paul Spielman, Peter Drakos, Stephen Hickman, Susan Lutz, Katie Boyle, Amber Falconer, Ann Robinson-Tait, Nicholas Davatzes, Peter Rose, Ernie Majer, and Steve Jarpe. 2012. Hydraulic stimulation of Well 27-15, Desert Peak Geothermal Field, Nevada, USA. Paper presented at the Thirty-Seventh Workshop on Geothermal Reservoir Engineering, Stanford, CA.

Cooper, J.R. 2007. Revised release on the IAPWS Industrial Formation 1997 for the thermodynamic properties of water and steam, International Association for the Properties of Water and Steam.

Craig, D. P., T. Hoang, H. Li, J. Magness, C. Ginn, V. Auzias. 2021. Defining Hydraulic Fracture Geometry Using Image Logs Recorded in the Laterals of Horizontal Infill Wells. Paper URTeC-5031-MS presented at the Unconventional Resources Technology Conference, Houston, TX.

Dontsov, E. V., and R. Suarez-Rivera. 2020. Propagation of multiple hydraulic fractures in different regimes. International Journal of Rock Mechanics & Mining Sciences 128:104270.

Dontsov, Egor, Christopher Hewson, and Mark McClure. 2022. A new crack propagation algorithm that enables accurate simulation of propagation across thin layers in a practical field-scale fracturing model. Paper SPE 209146-MS presented at the SPE Hydraulic Fracturing Technology Conference, The Woodlands, TX.

England, Kevin, and John McLennan. 2023. Stimulation plan between wells 16A(78-32) and 16B(78-32). Prepared for the U.S. Department of Energy Office of Energy Efficiency and Renewable Energy. Contract DE-EE0007080.

Evans KF, Moriya H, Niitsuma H, Jones RH, Phillips WS, Genter A, et al. Microseismicity and permeability enhancement of hydrogeologic structures during massive fluid injections into granite at 3 km depth at the Soultz HDR site. Geophys J Int 2005;160:389-412.

Fei, Fan, Andre Costa, John E. Dolbow, Randolph R. Settgast, and Matteo Cusini. 2023. Phase-Field Simulation of Near-Wellbore Nucleation and Propagation of Hydraulic Fractures in Enhanced Geothermal Systems (EGS). Paper presented at the 57th US Rock Mechanics/Geomechanics Symposium, Santa Fe, NM.

Fu, Wei, Brandon C. Ames, Andrew P. Bunger, Alexei A. Savitski. 2016. Impact of partially cemented and non-persistent natural fractures on hydraulic fracture propagation. 49: 4519-4526.

Fu, Pengcheng, et al. 2022. Close observations of hydraulic fracturing at EGS Collab Experiment 1: Fracture trajectory, microseismic interpretations, and the role of natural fractures. JGR Solid Earth, 10.1029/2020JB020840.

Gale, Julia F. W., Sara J. Elliott, and Stephen E. Laubach. 2018. Hydraulic fractures in core from stimulated reservoirs: Core fracture description of the HFTS slant core, Midland Basin, West Texas. Paper presented at the Unconventional Resources Technology Conference, Houston, TX.

Gale, Julia F. W., Sara J. Elliott, John Z. Li, and Stephen E. Laubach. 2019. Natural Fracture Characterization in the Wolfcamp Formation at the Hydraulic Fracture Test Site (HFTS), Midland Basin, Texas. Paper URTeC-2019-644-MS presented at the Unconventional Resources Technology Conference, Denver, CO.

Hawkins, Adam J., Danni Tang, Ritwick Sinha, Sean A. Fulcher, Sarah Hormozi, Patrick M. Fulton, Christopher A. Alabi, Uli B. Wiesner, Jefferson W. Tester. 2023. Active Tracers for Hydraulic Control of Cooled Short Circuits. Paper presented at the 48th Workshop on Geothermal Reservoir Engineering, Stanford, CA.

Lee, Sang H., and Ahmad Ghassemi. 2023. Modeling and Analysis of Stimulation and Fluid Flow in the Utah FORGE Reservoir. Paper presented at the 48th Workshop on Geothermal Reservoir Engineering, Stanford, CA.

Glauser, W., McLennan, J., Walton, I., 2013. Do perforated completions have value for engineered geothermal systems. In: Bunger, A., McLennon, J., Jeffrey, R.(Eds.), Effective and Sustainable Hydraulic Fracturing. InTech

Lawrence Berkeley National Laboratory. (2023). EGS Collab Experiment 2: Hydraulic Pressure Test Results [data set]. Retrieved from https://dx.doi.org/10.15121/1988394.

Lowry, Thomas S., Elena A. Kalinina, Teklu Hadgu, Katherine A. Klise, Leonard A. Malczynski. 2014. Economic Valuation of Directional Wells for EGS Heat Extraction. Paper presented at the Thirty-Ninth Workshop on Geothermal Reservoir Engineering, Stanford University.

Maity, Debotyam, and Jordan Ciezobka. 2020. A Data Analytics Framework for Cored Fracture Imaging and Novel Characterization Workflow - Application on Samples from Hydraulic Fracturing Test Site HFTS in the Midland Basin. Paper SPE-199754-MS presented at the Hydraulic Fracturing Technology Conference and Exhibition, The Woodlands, TX.

McClure, Mark W., Roland N. Horne. 2014a. An Investigation of Stimulation Mechanism in Enhanced Geothermal Systems. International Journal for Rock Mechanics and Mining Sciences 72: 242-260.

McClure, Mark, and Roland Horne. 2014b. Characterizing hydraulic fracturing with a tendency-for-shear-stimulation test. SPE Reservoir Evaluation & Engineering 17, 233-243.

McClure, Mark, Charles Kang, and Garrett Fowler. 2022. Optimization and Design of Next-Generation Geothermal Systems Created by Multistage Hydraulic Fracturing. SPE-209186-MS. Paper presented at the SPE Hydraulic Fracturing Technology Conference and Exhibition, The Woodlands, TX.

McClure, Mark. 2023a. Calibration Parameters Required to Match the Utah FORGE 16A(78)-32 Stage 3 Stimulation with a Planar Fracturing Model. Paper presented at the 48th Workshop on Geothermal Reservoir Engineering, Stanford, CA.

McClure, Mark. 2023b. Thermoelastic fracturing and buoyancy-driven convection: Surprising sources of longevity for EGS circulation. arXiv:2308.02761.

McClure, Mark, Charles Kang, Chris Hewson, Soma Medam, Egor Dontsov, and Ankush Singh. 2023. ResFrac Technical Writeup. 14th Edition. arXiv:1804.02092.

McLennan, John, Kevin England, Peter Rose, Joseph Moore and Ben Barker. 2023. Stimulation of a High-Temperature Granitic Reservoir at the Utah FORGE Site, SPE-212346-MS, Paper presented at the SPE Hydraulic Fracturing Technology Conference and Exhibition, The Woodlands, TX.

Moore, Joseph, John McLennan, Kristine Pankow, Stuart Simmons, Robert Podgorney, Philip Wannamaker, Pengju Xing, and Clay Jones. 2023. Current activities at the Utah Frontier Observatory for Research in Geothermal Energy (FORGE): A laboratory for characterizing, creating and sustaining Enhanced Geothermal Systems. Paper presented at the 48th Workshop on Geothermal Reservoir Engineering, Stanford, CA.

Norbeck, Jack H., and Timothy M. Latimer. 2023. Commercial-scale demonstration of a first-of-a-kind Enhanced Geothermal System. EarthArXiv. https://doi.org/10.31223/X52X0B.

Podgorney, Robert, Lynn Munday, Jerry Liu, Aleta Finnila, Branko Damjanac, Pengju Xing, and Zorica Radakovic-Guzina. 2023. Thermal-Hydraulic-Mechanical (THM) Modeling of Fluid Flow and Heat/Tracer Transport Between Injection and Production Wells at the Utah FORGE Site. Paper presented at the 48th Workshop on Geothermal Reservoir Engineering, Stanford, CA.

Raterman, Kevin T., Helen E. Farrell, Oscar S. Mora, Aaron L. Janssen, Gustavo A. Gomez, Seth Busetti, Jamie McEwen, Michael Davidson, Kyle Friehauf, James Rutherford, Ray Reid, Ge Jin, Baishali Roy, and Mark Warren. 2017. Sampling a Stimulated Rock Volume: An Eagle Ford Example. Paper presented at the Unconventional Resources Technology Conference, Austin, TX.

Raterman, Kevin T., Yongshe Liu, and Logan Warren. 2019. Analysis of a drained rock volume: An Eagle Ford example. Paper presented at the Unconventional Resources Technology Conference, Denver, CO.

McClure, Irvin, England, and McLennan

Ratnayake, Ruwantha, and Ahmad Ghassemi. 2023. Modeling of fiber optic strain responses to shear deformation of fractures. URTeC: 3852059. Paper presented at the Unconventional Resources Technology Conference, Denver, CO.

Shahri, Mojtaba, Andrew Tucker, Craig Rice, Zach Lathrop, Dave Ratcliff, Mark McClure, and Garrett Fowler. 2021. High fidelity fibre-optic observations and resultant fracture modeling in support of planarity. Paper SPE-204172-MS presented at the Hydraulic Fracturing Technology Conference and Exhibition, The Woodlands, TX.

Shiozawa, Sogo, Mark McClure. 2014. EGS Designs with Horizontal Wells, Multiple Stages, and Proppant. Paper presented at the Thirty-Ninth Workshop on Geothermal Reservoir Engineering, Stanford, CA.

Tarasovs, S., and A. Ghassemi. 2010. A study of propagation of cooled cracks in a geothermal reservoir. GRC Transactions 34.

Titov, A., S. Dadi, G. Galban, J. Norbeck, M. Almasoodi, K. Pelton, C. Bowie, J. Haffener, and K. Haustveit. 2024. Optimization of Enhanced Geothermal System operations using distributed fiber sensing and offset pressure monitoring. Paper SPE-217810-MS presented at the SPE Hydraulic Fracturing Technology Conference and Exhibition, The Woodlands, TX.

Ugueto, Gustavo, Paul Huckabee, Magdelena Wojtaszek, Talib Daredia, and Alan Reynolds. 2019a. New near-wellbore insights from fiber optics and downhole pressure gauge data. SPE-194371-MS. SPE Hydraulic Fracturing Technology Conference and Exhibition, The Woodlands, TX.

Ugueto, Gustavo A., Felix Todea, Talib Daredia, Magdalena Wojtaszek, Paul T. Huckabee, Alan Reynolds, Carson Laing, and J. Andres Chavarria. 2019b. Can you feel the strain? DAS strain fronts for fracture geometry in the BC Montney, Groundbirch. Paper SPE-195943-MS presented at the Annual Technical Conference and Exhibition, Calgary, Alberta.

Ugueto, Gustavo A., Magdalena Wojtaszek, Paul T. Huckabee, Alexei A. Savitski, Artur Guzik, Ge Jin, J. Andres Chavarria, Kyle Haustveit. 2021. An integrated view of hydraulic induced fracture geometry in Hydraulic Fracture Test Site 2. Paper URTeC: 5396 presented at the Unconventional Resources Technology Conference, Houston, TX.

Ugueto, Gustavo, Kan Wu, Ge Jin, Zhishuai Zhang, Jackson Haffener, Shahri Mojtaba, David Ratcliff, Rob Bohn, Andres Chavarria, Yinghui Wu, Artur Guzik, Aishwarya Srinivasan, Richard Gibson, and Alexei Savitski. 2023. A catalogue of fiber optics strain-rate fracture driven interactions. SPE-212370-MS. Paper presented at the SPE Hydraulic Fracturing Technology Conference and Exhibition, The Woodlands, TX.

Weng X, Kresse O, Cohen C-E, Wu R, Gu H. 2011. Modeling of hydraulic-fracture-network propagation in a naturally fractured formation. SPE Production & Operations 26, 368-80.

Xing, Pengju, Branko Damjanac, Zorica Radakovic-Guzina, Maurilio Torres, Aleta Finnila, Robert Podgorney, Joseph Moore, John McLennan. 2023. Comparison of modeling results with data recorded during field stimulations at Utah FORGE site. Paper presented at the 48th Workshop on Geothermal Reservoir Engineering, Stanford, CA.